



# The tidal evolution of the Fornax dwarf spheroidal and its globular clusters

Alexandra Borukhovetskaya, Raphaël Errani, Julio Navarro, Azadeh Fattahi,  
Isabel Santos-Santos

## ► To cite this version:

Alexandra Borukhovetskaya, Raphaël Errani, Julio Navarro, Azadeh Fattahi, Isabel Santos-Santos. The tidal evolution of the Fornax dwarf spheroidal and its globular clusters. Monthly Notices of the Royal Astronomical Society, 2022, 509, pp.5330-5339. 10.1093/mnras/stab2912 . hal-03390813

**HAL Id: hal-03390813**

**<https://hal.science/hal-03390813>**

Submitted on 21 Apr 2023

**HAL** is a multi-disciplinary open access archive for the deposit and dissemination of scientific research documents, whether they are published or not. The documents may come from teaching and research institutions in France or abroad, or from public or private research centers.

L'archive ouverte pluridisciplinaire **HAL**, est destinée au dépôt et à la diffusion de documents scientifiques de niveau recherche, publiés ou non, émanant des établissements d'enseignement et de recherche français ou étrangers, des laboratoires publics ou privés.

# The tidal evolution of the Fornax dwarf spheroidal and its globular clusters

Alexandra Borukhovetskaya<sup>1</sup>,<sup>1</sup>★ Raphaël Errani,<sup>1,2</sup> Julio F. Navarro,<sup>1</sup> Azadeh Fattahi<sup>3</sup>  
and Isabel Santos-Santos<sup>1</sup>

<sup>1</sup>Department of Physics and Astronomy, University of Victoria, Victoria, BC V8P 5C2, Canada

<sup>2</sup>Observatoire Astronomique, Université de Strasbourg, CNRS, 11 rue de l'Université, F-67000 Strasbourg, France

<sup>3</sup>Institute for Computational Cosmology, Department of Physics, University of Durham, South Road, Durham DH1 3LE, UK

Accepted 2021 October 1. Received 2021 October 1; in original form 2021 March 30

## ABSTRACT

The dark matter content of the Fornax dwarf spheroidal galaxy inferred from its kinematics is substantially lower than expected from LCDM cosmological simulations. We use  $N$ -body simulations to examine whether this may be the result of Galactic tides. We find that, despite improved proper motions from the *Gaia* mission, the pericentric distance of Fornax remains poorly constrained, mainly because its largest velocity component is roughly antiparallel to the solar motion. Translating Fornax's proper motion into a Galactocentric velocity is, thus, sensitively dependent on Fornax's assumed distance: the observed distance uncertainty,  $\pm 8$  per cent, implies pericentric distances that vary between  $r_{\text{peri}} \sim 50$  and  $\sim 150$  kpc. Our simulations show that for  $r_{\text{peri}}$  in the lower range of that estimate, an LCDM subhalo with maximum circular velocity  $V_{\text{max}} = 40 \text{ km s}^{-1}$  (or virial mass  $M_{200} \approx 10^{10} M_{\odot}$ , as expected from LCDM) would be tidally stripped to  $V_{\text{max}} \sim 23 \text{ km s}^{-1}$  over 10 Gyr. This would reduce the dark mass within the Fornax stellar half-mass radius to about half its initial value, bringing it into agreement with observations. Tidal stripping affects mainly Fornax's dark matter halo; its stellar component is affected little, losing less than 5 per cent of its initial mass in the process. We also explore the effect of Galactic tides on the dynamical friction decay times of Fornax's population of globular clusters (GCs) and find little evidence for substantial changes, compared with models run in isolation. A population of GCs with initial orbital radii between 1 and 2 kpc is consistent with the present-day spatial distribution of Fornax GCs, despite assuming a cuspy halo. Neither the dark matter content nor the spatial distribution of GCs of Fornax seems inconsistent with a simple model where Fornax inhabits a tidally stripped cuspy cold dark matter halo.

**Key words:** galaxies: dwarf – galaxies: evolution – dark matter.

## 1 INTRODUCTION

The standard model of cosmology, Lambda Cold Dark Matter (LCDM), predicts structures to form hierarchically. In this paradigm, large self-bound structures (haloes) form through the accretion and mergers of smaller ones (subhaloes), which in turn form from small-scale density perturbations in the early Universe (White & Rees 1978). Massive haloes allow stars to form in their centres from cooling of accreted gas: the more massive the host halo, the more stars it is able to form. In low-mass haloes ( $\lesssim 10^9 M_{\odot}$ ), however, cosmic reionization and energetic feedback from stellar evolution reduce substantially a halo's ability to form stars (Bullock, Kravtsov & Weinberg 2000; Benson et al. 2002; Somerville 2002).

This implies that a steep non-linear relation between the dark matter masses of the smallest haloes and their stellar masses is expected in LCDM, a prediction that has been supported by both semi-analytic techniques such as ‘abundance-matching’ (Guo et al. 2010; Behroozi, Wechsler & Conroy 2013; Moster, Naab & White 2013), and by direct cosmological hydrodynamical simulations (e.g. the Illustris and EAGLE simulations, Vogelsberger et al. 2014; Schaye et al. 2015, respectively).

More specifically, on the scale of dwarf galaxies, simulations predict that galaxies with stellar masses  $M_{\text{str}} \sim 2.4 \times 10^7 M_{\odot}$ , like the Fornax dwarf spheroidal (dSph) (see Table 3), should form in a halo with a virial<sup>1</sup> mass of at least  $M_{200} \approx 10^{10} M_{\odot}$  (Wang et al. 2015; Fattahi et al. 2018; Garrison-Kimmel et al. 2019; Munshi et al. 2021).

In LCDM, where the dark matter halo mass distribution is adequately approximated by Navarro–Frenk–White profiles (hereafter NFW; Navarro, Eke & Frenk 1996; Navarro et al. 1997), this virial mass corresponds to a halo with maximum circular velocity,  $V_{\text{max}} = 39.6 \text{ km s}^{-1}$ , for a ‘concentration’ parameter  $c = 12.5$  (Ludlow et al. 2016). The mass profile of such a halo is fully specified, enabling predictions of the dark mass enclosed within the galaxy stellar half-mass radius,<sup>2</sup> where observational constraints are tightest (Walker, Mateo & Olszewski 2009; Wolf et al. 2010). In the case of the Fornax dSph,  $r_{1/2} \approx 1 \text{ kpc}$ , and observations suggest a total enclosed mass of  $M_{\text{tot}}(< r_{1/2}) \approx 9 \times 10^7 M_{\odot}$  (or, equivalently, a circular velocity

<sup>1</sup>We define the virial mass as the mass enclosed within the radius of overdensity 200 times the critical density required for closure,  $\rho_{\text{crit}} = 3H^2/8\pi G$ , where  $H(z)$  is Hubble's constant and  $H_0 = H(0) = 67.74 \text{ km Mpc}^{-1} \text{ s}^{-1}$  (Planck Collaboration et al. 2016)

<sup>2</sup>We shall use uppercase  $R_{1/2}$  to denote projected half-mass radii and lowercase  $r_{1/2}$  to denote deprojected, 3D, radii. We shall usually assume  $R_{1/2} = (3/4)r_{1/2}$ , as appropriate for spherical systems, unless otherwise noted.

★ E-mail: [asya@uvic.ca](mailto:asya@uvic.ca)

of  $V_c(r_{1/2}) \approx 20 \text{ km s}^{-1}$ , much larger than the mass in the stellar component (Fattahi et al. 2016a; Read, Walker & Steger 2019).

For an NFW halo of average concentration, the latter constraint implies  $V_{\text{max}} \sim 25 \text{ km s}^{-1}$ , substantially below that expected from the cosmological simulations referenced above. The disagreement is amplified by the steep non-linear dependence of stellar mass on halo mass in this regime. Indeed, in LCDM haloes with  $V_{\text{max}} \sim 25 \text{ km s}^{-1}$  are expected to harbour dwarfs with  $M_{\text{str}} \sim 10^6 M_{\odot}$ , more than an order of magnitude less luminous than Fornax. If such low-mass haloes were to harbour galaxies as massive as Fornax, one would expect nearly an order of magnitude more Fornax-like dwarfs than observed in the Local Group.

The unexpectedly low dark matter content of Fornax is often cited as suggesting the presence of a constant-density ‘core’ in the inner halo density profile (see e.g. Walker & Peñarrubia 2011; Amorisco, Agnello & Evans 2013). Such cores may result from the supernova-driven cycling of baryons in and out of the inner regions of a halo during galaxy formation (see e.g. Navarro et al. 1996; Read & Gilmore 2005; Pontzen & Governato 2012; Di Cintio et al. 2014), but their occurrence is not universally accepted.

In the absence of cores, one would need to argue that the dark matter content of Fornax has been eroded somewhat by Galactic tides. Fornax’s stellar component shows no obvious sign of tidal disturbance, however, but tidal stripping is expected to affect mainly the more extended dark matter component (see e.g. Peñarrubia, Navarro & McConnachie 2008). Tidal stripping may, thus, lead to a reduction of the dark matter content of a dwarf without affecting much the stellar component. This has been argued by Genina et al. (2020), for example, who selected dwarf galaxies with orbital properties similar to Fornax in the APOSTLE simulations, and showed that many such satellites lose more than half of their mass from within their innermost  $\sim 1 \text{ kpc}$ .

Although plausible, the main obstacle to this tidal-stripping interpretation is Fornax’s large Galactocentric distance ( $\sim 149 \text{ kpc}$ ; Pietrzyński et al. 2009), together with early estimates of its orbital eccentricity, which suggested a low-eccentricity orbit (see; e.g. Piatek et al. 2002; Dinescu et al. 2004; Battaglia, Sollima & Nipoti 2015, and references therein). At such distance, it would be unlikely for Fornax to have been affected much by Galactic tides if it was on a nearly circular orbit.

Besides its unexpectedly low dark matter content, Fornax has long been argued to pose an additional problem for LCDM. This relates to its globular cluster (GC) spatial distribution, which seems inconsistent with the fact that their dynamical friction orbital decay time-scales appear to be much shorter than their ages (Tremaine 1976; Hernandez & Gilmore 1998). Goerdt et al. (2006) proposed that the problem could be resolved if the structure of the Fornax dark halo had a sizeable constant density core, a result echoed in subsequent work (see e.g. Read et al. 2006; Cole et al. 2012; Petts, Gualandris & Read 2015).

More recent work, however, has argued for a different explanation that does not require a core. Meadows et al. (2020), for example, report that GCs have similar dynamical friction time-scales in both cuspy and cored haloes normalized to match observed constraints on  $M_{\text{tot}}(< r_{1/2})$ . More precisely, in either case, GCs are driven by dynamical friction to well-defined terminal radii in about the same time. The difference is where they end up: GCs are driven close to the centre in the case of a cusp but ‘stall’ at about one-third of the core radius<sup>3</sup> ( $\sim 300 \text{ pc}$  for a  $\sim 1 \text{ kpc}$  core). Because there is no

clearcut evidence for such characteristic common radius for GCs in Fornax, this suggests that, if dynamical friction has indeed affected GC orbits, its effects have been mild and might still be ongoing.

In this interpretation, Fornax GCs were likely formed or accreted into Fornax on orbits with radii somewhat larger than where they are today (Angus & Diaferio 2009; Boldrini, Mohayaee & Silk 2019). Indeed, dynamical friction time-scales depend sensitively on orbital radius, and it is relatively easy to accommodate the present-day configuration of GCs if their initial radii were just outside Fornax’s half-light radius,  $r_{1/2}$  (Meadows et al. 2020). Would such clusters survive stripping by Galactic tides if the latter are indeed responsible for the low dark matter content of Fornax?

A further alternative is that GC orbital decay may have been affected by the ‘dynamical stirring’ and halo mass-loss that could arise from Galactic tides (Oh, Lin & Richer 2000). If so, the effect of Galactic tides could, in principle, serve to solve the two problems at once, reconciling the low dark matter content of Fornax, as well as the unexpectedly long decay time-scales of its GCs, with the predictions of LCDM.

We explore these questions here using a series of controlled, high-resolution  $N$ -body simulations of the tidal evolution of Fornax. This paper is structured as follows: in Section 2, we discuss our numerical setup, with Section 2.1 detailing our Milky Way host model, Section 2.2 describes our choice of orbital parameters, and Sections 2.3 and 2.4 detail our halo model and  $N$ -body realizations. Section 3 presents our results, beginning with the dynamical evolution of dark matter in Section 3.1 and ending with the effect of tides on the stellar component (Section 3.2) and GCs (Section 3.3). We conclude with a summary of our conclusions in Section 4.

## 2 NUMERICAL SETUP

This section outlines the numerical setup of the  $N$ -body simulations used to follow the tidal evolution of our Fornax model in the gravitational potential of the Milky Way.

### 2.1 Galaxy model

The Milky Way is modelled as an analytical, static potential, consisting of an axisymmetric two-component Miyamoto & Nagai (1975) disc, a Hernquist (1990) bulge and an NFW dark matter halo. The model parameters (summarized in Table 1) are as in Errani & Peñarrubia (2020), chosen to approximate the McMillan (2011) model with circular velocity  $V_c = 240 \text{ km s}^{-1}$  at the solar circle  $R_0 = 8.29 \text{ kpc}$ . The thick and thin discs are each parametrized by a disc mass  $M$ , a scale length  $a_d$  and a scale height  $b_d$ ; similarly, the bulge is described by a total mass  $M$  and scale length  $a$ . The NFW model for the Milky Way dark matter halo can be characterized by a scale radius  $r_s$  and the mass enclosed within that radius,  $M_s$ . These parameters are listed in Table 1.

### 2.2 Orbits

The orbit of Fornax in the Milky Way potential is specified by its present-day Galactocentric position and velocity, as inferred from its sky position, radial velocity, distance, and proper motion. Of these, the sky position and radial velocity  $v_r = 55.3 \pm 0.3 \text{ km s}^{-1}$  have negligible uncertainties (see e.g. Fritz et al. 2018). The heliocentric distance and proper motions, on the other hand, are known to

<sup>3</sup>The core radius is defined here as the distance where the projected density of the halo drops to 1/2 of its central value. Since this convention is not always

followed, care is needed when comparing quantitative results for the ‘stall radius’ from different authors.

**Table 1.** Parameters of the analytical, static Milky Way potential used in this study. The model is a spherical re-parametrization of the McMillan (2011) model, as discussed in Errani & Peñarrubia (2020).

Component	Functional form			
Disc (thin)	Miyamoto & Nagai (1975)	$M = 5.9 \times 10^{10} M_{\odot}$	$a_d = 3.9 \text{ kpc}$	$b_d = 0.31 \text{ kpc}$
Disc (thick)	Miyamoto & Nagai (1975)	$M = 2.0 \times 10^{10} M_{\odot}$	$a_d = 4.4 \text{ kpc}$	$b_d = 0.92 \text{ kpc}$
Bulge	Hernquist (1990)	$M = 2.1 \times 10^{10} M_{\odot}$	$a = 1.3 \text{ kpc}$	
DM Halo	Navarro, Frenk & White (1997)	$M_{200} = 1.15 \times 10^{12} M_{\odot}$	$r_s = 20.2 \text{ kpc}$	$c = r_{200}/r_s = 9.5$

$\sim 10$  per cent accuracy:  $d = 147 \pm 12.0 \text{ kpc}$  (Pietrzyński et al. 2009), and  $\mu_{\alpha^*} = 0.374 \pm 0.035 \text{ mas/yr}$ ,  $\mu_{\delta} = -0.401 \pm 0.035 \text{ mas yr}^{-1}$  (Fritz et al. 2018).<sup>4</sup>

These uncertainties result in a fairly broad distribution of possible pericentric and apocentric distances. This is shown in Fig. 1, where we plot in the top two panels, as a function of the assumed distance, the resulting pericentric and apocentric distances in the potential described in Section 2.1. The pericentric distance, the parameter most critical in respect to the effect of Galactic tides, ranges from  $\sim 50 \text{ kpc}$  at the 16th percentile to  $\sim 130 \text{ kpc}$  at the 84th percentile of the distribution obtained by varying all parameters within their uncertainty range. In other words, a  $\sim 10$  per cent uncertainty in distance translates into more than a factor of two uncertainty in pericentric distance.

This striking sensitivity of the pericentric distance on assumed distance is due to Fornax’s direction of motion, which lies approximately antiparallel to the solar motion around the Galaxy. As a result, Fornax’s velocity in the heliocentric frame is mainly tangential and quite large,  $\sim 350 \text{ km s}^{-1}$ , far exceeding Fornax’s total speed in the Galactocentric reference frame (see Table 2).

Since proper motions are measured in the heliocentric frame, an  $\sim 8$  per cent uncertainty in distance implies a large tangential velocity uncertainty, roughly 21 per cent in terms of the Galactocentric tangential velocity. This is shown in the bottom panel of Fig. 1, where we show the effect of distance on the inferred heliocentric and Galactocentric tangential velocities of Fornax. Because the Galactocentric tangential velocity is not tightly constrained, the orbital pericentre is likewise poorly determined.

Because of this uncertainty, we have explored three different orbits, with orbital properties as given by the open symbols in Fig. 1. These orbits have notably different pericentric distances,  $r_{\text{peri}} = 53.1, 90.5$ , and  $128 \text{ kpc}$ , and the corresponding orbits are, hereafter, referred to as orbits 1, 2, and 3, respectively, with main parameters listed in Table 2. Initial conditions for the  $N$ -body runs are obtained by integrating those orbits backwards in time for 10 Gyr. The shape of the resulting orbits are shown in Fig. 2. Note that the three orbits are nearly polar, and close to the  $Y$ - $Z$  plane.<sup>5</sup>

### 2.3 Fornax model

We model the Fornax dSph halo as an equilibrium  $N$ -body realization of an NFW density profile

$$\rho_{\text{NFW}}(r) = \frac{M_{200}}{4\pi r_s^3} \frac{(r/r_s)^{-1}(1+r/r_s)^{-2}}{[\ln(1+c) - c/(1+c)]}. \quad (1)$$

<sup>4</sup>Where with  $\mu_{\alpha^*}$ , we designate the proper motion in  $\alpha$  including the  $\cos(\delta)$  factor.

<sup>5</sup>We use a co-ordinate system where the Sun is located at  $(X, Y, Z)_{\odot} = (-8.3 \text{ kpc}, 0, 0)$ , and the velocity of the local standard of rest is in the positive  $Y$  direction.

This profile is fully specified by two parameters; e.g. a virial mass,  $M_{200}$ , and concentration,  $c$ , or, alternatively, by a maximum circular velocity,  $V_{\text{max}}$ , and the radius at which it is achieved,  $r_{\text{max}}$ . The latter is often favoured since, unlike the former, it is defined independently of redshift and may be more directly compared with observations.

Cosmological hydrodynamical simulations have shown that  $V_{\text{max}}$  correlates strongly with galaxy stellar mass,  $M_{\text{str}}$ , as shown, for example, in Fig. 3 for results from the APOSTLE suite of Local Group simulations (Sawala et al. 2016; Fattahi et al. 2016b).

We use the empirical fit from Fattahi et al. (2018)

$$M_{\text{str}}/M_{\odot} = m_0 v^{\alpha} \exp(-v^{\gamma}), \quad (2)$$

where  $v = V_{\text{max}}/50 \text{ km s}^{-1}$ , and  $(m_0, \alpha, \gamma) = (3.0 \times 10^8, 3.36, -2.4)$ . This fit is shown in Fig. 3, along with measured stellar masses and maximum circular velocities of isolated galaxies in the APOSTLE simulation.

We adopt a stellar mass for Fornax of  $M_{\text{str}} = 2.39 \times 10^7 M_{\odot}$ , computed from the apparent  $V$ -band luminosity as in Irwin & Hatzidimitriou (1995), the distance modulus of Pietrzyński et al. (2009) and the stellar mass-to-light ratio of Woo, Courteau & Dekel (2008). Equation (2) then suggests a maximum circular velocity of  $V_{\text{max}} = 39.6 \text{ km s}^{-1}$ . This assumes that tides have not affected Fornax’s stellar mass – an assumption which we shall see justified by our results, as discussed in Section 3.2.

The radius where the circular velocity peaks,  $r_{\text{max}}$ , may be calculated from the Ludlow et al. (2016) parametrization of the LCDM halo mass-concentration relation at redshift  $z = 0$ . As listed in Table 3, the resulting NFW profile has  $V_{\text{max}} = 39.6 \text{ km s}^{-1}$  and  $r_{\text{max}} = 8.0 \text{ kpc}$ , or, in terms of virial mass and concentration,  $M_{200} = 1.04 \times 10^{10} M_{\odot}$  and  $c = 12.5$ . This initial virial mass is roughly a factor of two lower than the average halo mass inferred for galaxies which host as many GCs as Fornax, but well within the scatter of that relation (see e.g. Forbes et al. 2018; Shao et al. 2020).

The  $N$ -body realization of the halo model is constructed with  $10^6$  particles ( $10^7$  in some cases, as specified in Section 3.3) using the ZENO<sup>6</sup> software package developed by Joshua Barnes at the University of Hawaii. This software provides routines for Monte Carlo sampling a given distribution function whereby a system in virial equilibrium may be generated. In order for the system to fully relax prior to introducing an external potential, the halo is run in isolation for 6 Gyr using the publicly available GADGET-2 simulation code (Springel 2005), as detailed below.

### 2.4 Simulation code

We use the  $N$ -body code GADGET-2 (Springel 2005) to evolve our  $N$ -body models. This code implements a hierarchical tree algorithm to compute gravitational interactions. Forces between particles are smoothed with a Plummer-equivalent softening length of  $\epsilon_p = 40 \text{ pc}$

<sup>6</sup><http://www.ifa.hawaii.edu/faculty/barnes/zeno/>



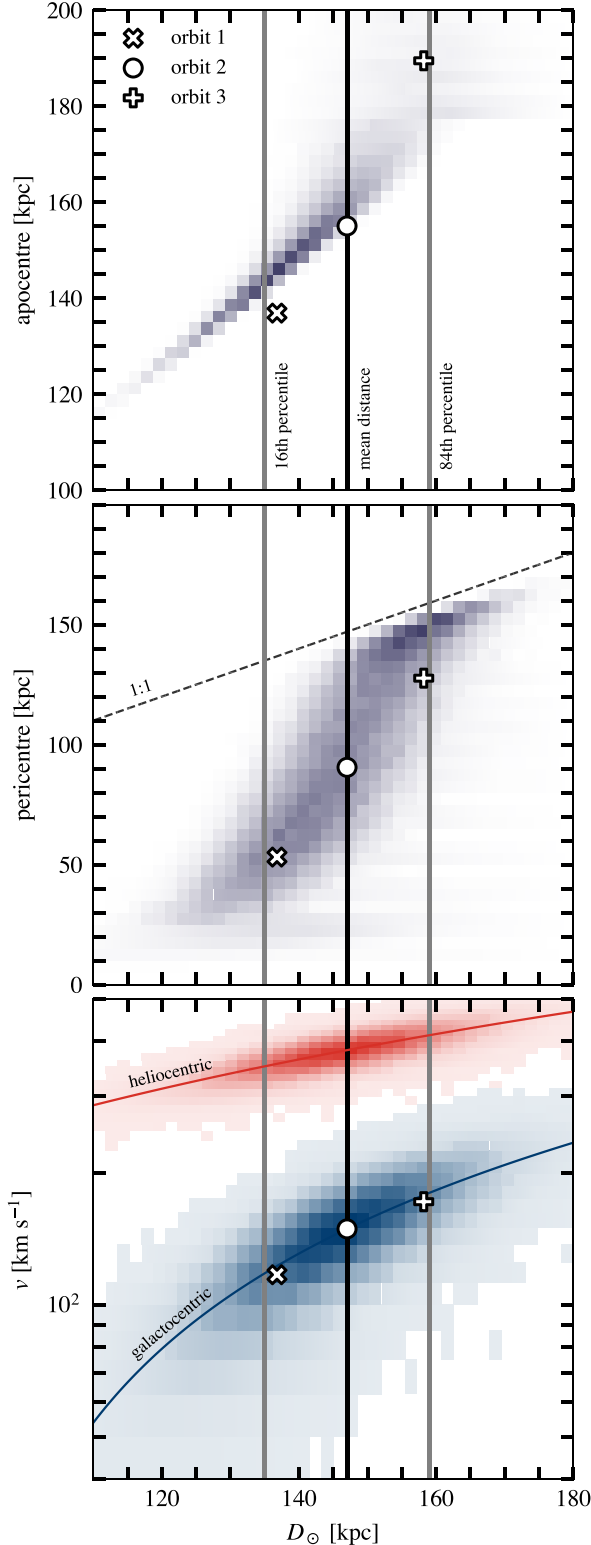


**Figure 1.** The apocentric (top panel) and pericentric (central panel) distance of Fornax as a function of heliocentric distance, varying the proper motions and radial velocity within the observed uncertainties. The properties corresponding to the three orbits of Table 2 are highlighted in each panel using white symbols (x, o, +). Vertical lines correspond to the median measured distance (black) as well as the 16th and 84th percentile (grey). The bottom panel shows the heliocentric (red) and galactocentric (blue) tangential velocities. Note that the distance uncertainty propagates to a large uncertainty in the Galactocentric velocity.

for  $N = 10^6$  and  $\epsilon_P = 13$  pc for  $N = 10^7$  particles. For each of the orbits described in Section 2.2, the  $N$ -body model is evolved on the respective orbit in the potential of Section 2.1 for  $\sim 10$  Gyr. We have also evolved the same  $N$ -body models in isolation to identify the smallest radius for which our mass profiles are numerically converged. Defining this as the innermost radius where circular velocities deviate by less than  $\sim 1$  percent from the target NFW profile, we consider our results converged outside  $r_{\text{conv}} = 450$  pc and  $r_{\text{conv}} = 140$  pc for our  $10^6$  or  $10^7$ -particle runs, respectively.

### 3 RESULTS

We present below the results of the evolution of our Fornax  $N$ -body model in the Galactic potential for each of the three orbits discussed above. We discuss first the stripping of dark matter, followed by a discussion of the stripping of a hypothetical embedded stellar component that matches Fornax's light distribution. We end with a discussion of how Galactic tides may affect the orbital decay of Fornax GCs.

#### 3.1 Dark matter stripping

Dashed lines in Fig. 4 show the evolution of the maximum circular velocity of our Fornax haloes for the three simulated orbits. Consistent with the findings of Hayashi et al. (2003) and Peñarrubia et al. (2008), as tides strip the system,  $V_{\text{max}}$  decreases continuously, with abrupt changes corresponding to pericentric passages.

As expected, the smaller the pericentre the stronger the tidal forces and thus the more significant the mass-loss. For orbit 1 ( $r_{\text{peri}} = 53$  kpc), the circular velocity at the half-light radius,  $V_{1/2} \equiv V_c(r_{1/2} = 1 \text{ kpc})$ , drops enough after just 4 Gyr to fall within the  $1\sigma$  interval around the observational estimate,  $20.2 \pm 2.8 \text{ km s}^{-1}$ , shown as a grey band in Fig. 4 (Fattahi et al. 2016a). For Orbit 1, even after  $\sim 10$  Gyr,  $V_{1/2}$  is still consistent with the observed value. The remnant halo in this case retains only 6 percent of its initial dark mass (yet still fairly well resolved, with more than  $2 \times 10^4$  particles within  $r_{\text{max}}$ ), and its  $V_{\text{max}}$  has dropped from  $\sim 40 \text{ km s}^{-1}$  to roughly  $23 \text{ km s}^{-1}$ . (The snapshots that match best the current Galactocentric distance of Fornax after  $\sim 10$  Gyr of evolution are indicated by symbols in Fig. 4.)

On the other hand, models on Orbits 2 and 3 ( $r_{\text{peri}} = 91$  and  $134$  kpc) do not lose enough mass for  $V_{1/2}$  to reach the  $1\sigma$  error band of the observationally inferred value, even after  $\sim 10$  Gyr of evolution.

The final circular velocity profiles are shown for the three orbits in Fig. 5. As shown in this figure, the final  $V_c$  profile of the tidally stripped halo on Orbit 1 matches well not only the Fattahi et al. (2016a) constraints on the mass enclosed within  $\sim 1$  kpc (red contours), but also – within  $2\sigma$  – the mass profile of Read et al. (2019) derived from a kinematic analysis of Fornax's stellar component (shaded band). Tighter observational constraints at small radii should help to further assess the viability of the tidally driven scenario proposed here.

Note, in particular, that the mass profile of the stripped halo differs from the NFW shape: the dotted curve in Fig. 5 shows an NFW profile with the same  $r_{\text{max}}$  and  $V_{\text{max}}$  as the final Fornax model profile on Orbit 1 (see e.g. Errani & Navarro 2020, for details). The Orbit 1 final profile is also in reasonable agreement with mass estimates from Walker & Peñarrubia (2011) and Amorisco et al. (2013), shown by the symbols with error bars in Fig. 5.

We conclude that tidal effects may very well reconcile the observed low dark matter content of Fornax with the relatively massive

**Table 2.** Current observational constraints, as well as parameters of the three orbits explored using  $N$ -body simulations in this study. Orbit 2 is the orbit corresponding to the median observed quantities. The current positions and velocities of Fornax corresponding to orbits 1, 2, and 3, expressed as 6D Cartesian coordinates, lie each within at most one standard deviation of the ones derived by Gaia Collaboration et al. (2018). Pericentres and apocentres are computed for the Milky Way potential model discussed in Section 2.1, while heliocentric and galactocentric coordinates are computed with solar parameters of Schönrich, Binney & Dehnen (2010).

Observation	$\alpha$	$\delta$	Distance (kpc)	$\mu_{\alpha^*}$ (mas yr $^{-1}$ )	$\mu_{\delta}$ (mas yr $^{-1}$ )	$v_r$ (km s $^{-1}$ )
	2 <sup>h</sup> 39 <sup>m</sup> 59 <sup>s</sup> .3 <sup>(1)</sup>	−34°26′57″ <sup>(1)</sup>	147 ± 12.0 <sup>(2)</sup>	0.374 ± 0.035 <sup>(3)</sup>	−0.401 ± 0.035 <sup>(3)</sup>	55.3 ± 0.3 <sup>(3)</sup>
	$X$	$Y$	$Z$	$V_X$	$V_Y$	$V_Z$
	(kpc)	(kpc)	(kpc)	(km s $^{-1}$ )	(km s $^{-1}$ )	(km s $^{-1}$ )
Heliocentric	−32.9	−50.9	−134	29.3	−377	75.5
Galactocentric	−41.2	−50.9	−134	40.4	−125	82.8
<sup>(1)</sup> McConnachie (2012), <sup>(2)</sup> Pietrzyński et al. (2009), <sup>(3)</sup> Fritz et al. (2018)						
Model parameters	Pericentre (kpc)	Apocentre (kpc)	Distance (kpc)	$\mu_{\alpha^*}$ (mas yr $^{-1}$ )	$\mu_{\delta}$ (mas yr $^{-1}$ )	$v_r$ (km s $^{-1}$ )
Orbit 1	53.1	137	137	0.384	−0.382	55.1
Orbit 2	90.5	155	147	0.374	−0.401	55.3
Orbit 3	128	189	158	0.390	−0.376	55.4

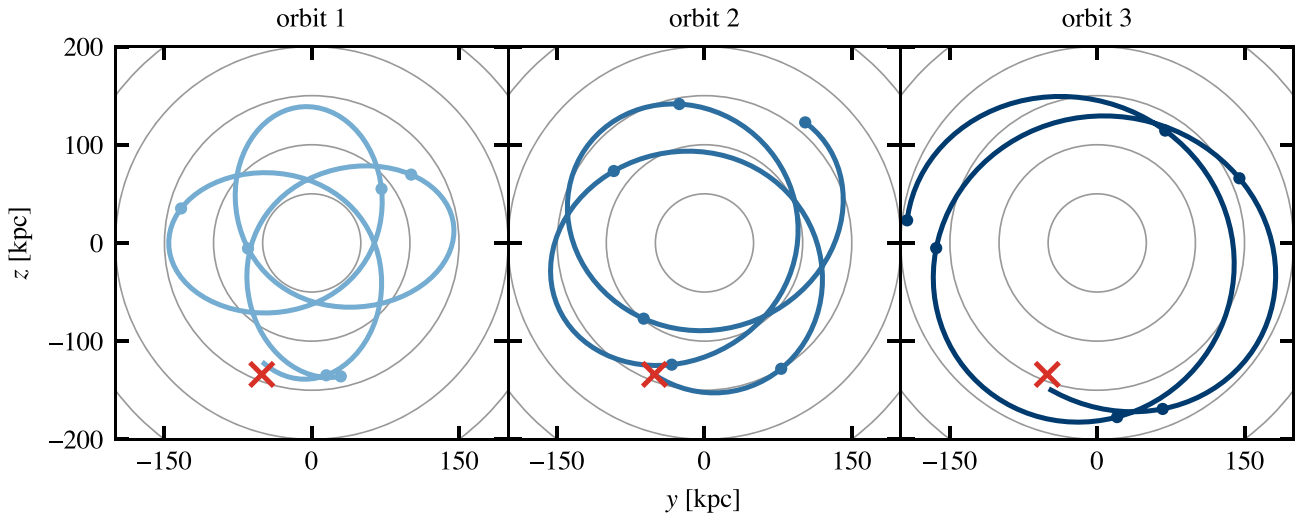


**Figure 2.** Projected trace on the  $Y, Z$  plane of the three orbits considered in this study (see Table 2). The current position of Fornax is indicated by a red cross. Intervals of 2 Gyr along the orbit are shown using filled circles.

halo suggested by current LCDM cosmological hydrodynamical simulations. This requires that Fornax is on an eccentric orbit with  $r_{\text{peri}}$  as small as  $\sim 50$  kpc, and that it has orbited the Milky Way potential for at least 4–5 Gyr. This is consistent with the observed proper motions if Fornax’s current distance is of order 140 kpc or less, a value well within the error bar on the current estimate of  $147 \pm 12$  kpc. Tighter constraints on Fornax’s distance would help to verify this prediction.

### 3.2 Stellar component stripping

As discussed in the previous section, Galactic tides are capable of substantially altering the internal distribution of dark matter in the Fornax dSph. We study next to what extent the same tides may affect Fornax’s stellar population, limiting this analysis to Orbit 1, which is subject to the strongest tides.

To begin, we shall assume that stars are collisionless tracers of the underlying dark matter potential. This is well-motivated by the large dark-to-stellar mass ratio of Fornax, as discussed in Section 1. We use the approach introduced by Bullock & Johnston (2005) to assign

stellar probabilities to each dark matter particle, using the publicly available<sup>7</sup> implementation of Errani & Peñarrubia (2020).

The initial stellar density profile is modelled as an Einasto profile (Einasto 1965),

$$\rho_E(r) = \rho_{E0} \exp \left[ - (r/a)^{1/n} \right], \quad (3)$$

with index  $n = 0.81$  and scale radius  $a = 0.44$  kpc. (The central density  $\rho_{E0}$  depends on the stellar mass-to-light ratio assumed, but it should be inconsequential provided the system is dark matter dominated throughout.)

These parameters have been chosen so that after  $\sim 10$  Gyr of evolution, the simulated stellar distribution of the remnant matches the currently observed stellar density profile. The initial and final stellar density profiles are shown in Fig. 6. The left-hand panel shows the simulated profiles in 3D, whereas the right-hand panel shows them in projection. These Sersic (1968) profiles fit very well the observed surface density of Fornax (circles with error bars, normalized to the central value) taken from Coleman et al. (2005).

<sup>7</sup><https://github.com/rerrani/nbody>

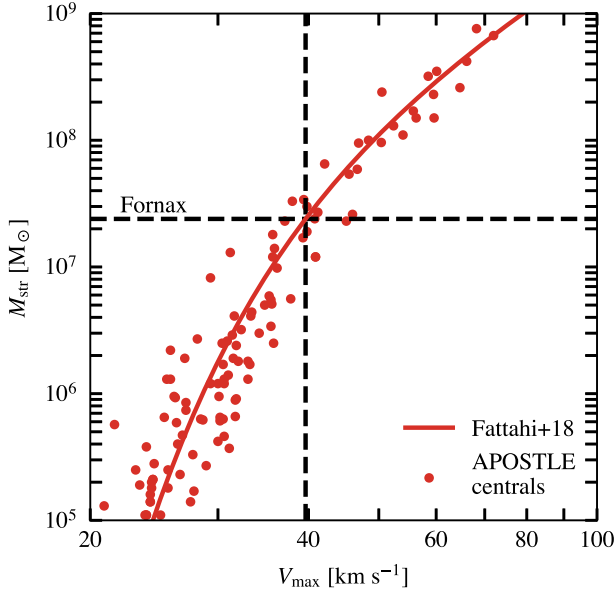


**Figure 3.** Stellar mass,  $M_{\text{str}}$ , versus maximum circular velocity,  $V_{\text{max}}$ , of central galaxies from the highest resolution level (L1) runs in the APOSTLE simulations as described in Fattahi et al. (2018). The red solid line is the average relation from that work (equation 2). Dashed lines indicate stellar mass and derived  $V_{\text{max}}$  for Fornax as listed in Table 3.

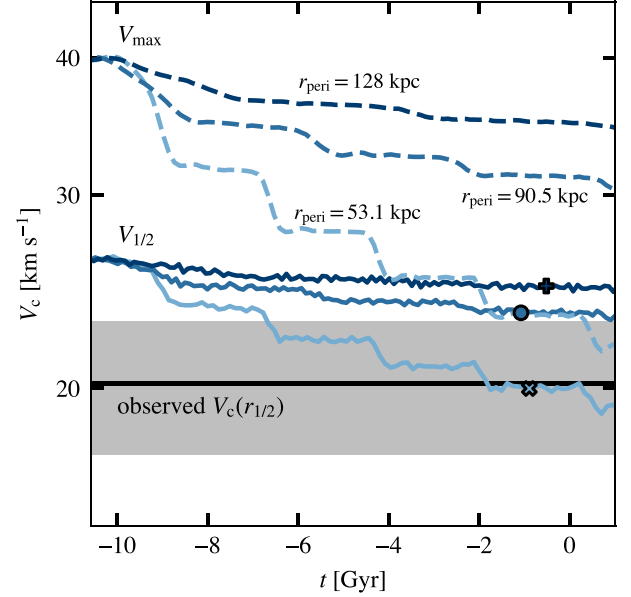
**Table 3.** Current properties of Fornax ( $M_{\text{str}}$ ,  $V_{1/2}$ ,  $r_{1/2}$ ) and inferred structural parameters at infall ( $V_{\text{max}}$ ,  $r_{\text{max}}$ ). The stellar mass is derived from the distance modulus of Pietrzyński et al. (2009), the V-band magnitude of Irwin & Hatzidimitriou (1995), and the stellar mass-to-light ratio of Woo et al. (2008). The maximum circular velocity at infall  $V_{\text{max}}$  is estimated from the stellar mass through equation (2), and the corresponding  $r_{\text{max}}$  is chosen to match the Ludlow  $z = 0$  mass–concentration relation (Ludlow et al. 2016). Half-light radius  $r_{1/2}$  and circular velocity  $V_{1/2}$  at the half-light radius are as in Fattahi et al. (2018).

$M_{\text{str}}$ ( $10^7 M_{\odot}$ )	$V_{\text{max, infall}}$ ( $\text{km s}^{-1}$ )	$r_{\text{max, infall}}$ (kpc)	$V_{1/2}$ ( $\text{km s}^{-1}$ )	$r_{1/2}$ (kpc)
2.39	39.6	7.99	$20.2 \pm 2.8$	$0.949^{+1.06}_{-1.00}$

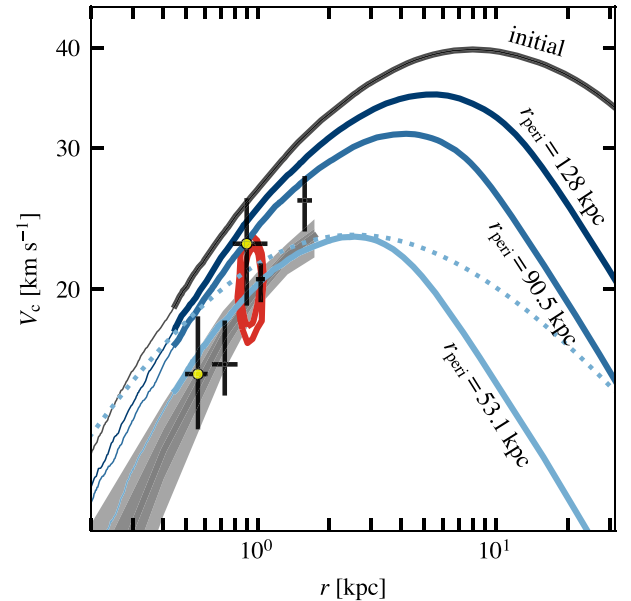
While tides have a significant effect on the dark matter content of Fornax, the effect of tides on the stellar density distribution is minor. More than 9 per cent of the initial stellar mass remains bound, and its half-mass radius increases only by  $\sim 25$  per cent over 10 Gyr of evolution. Battaglia et al. (2015) reached a similar conclusion, wherein more than 99 per cent of stellar particles remain bound, although they assumed a lower initial Fornax halo mass, and orbits with larger pericentric distances. The marginal stellar mass-loss corroborates our earlier assumption in Section 2.3: the current stellar mass of Fornax is essentially unchanged by the Galactic tides, and may, thus, be used to estimate the halo mass at infall.

Fig. 7 shows the distribution of stars in the Fornax model as projected on the sky.<sup>8</sup> The left-hand panel shows an area of  $5 \times 5 \text{ deg}^2$  centred on Fornax, and shows no obvious signature of tidal effects, consistent with the recent analysis of Wang et al. (2019), who report no tidal signature in the innermost  $2^\circ$ . Only far from the main body of the galaxy do signs of tidal distortions become evident.

<sup>8</sup>An implementation of the tessellation method used to generate the surface brightness map is publicly available at <https://github.com/asya-b/voronoi>.



**Figure 4.** Evolution of the circular velocity of the Fornax halo for the three different orbits, shown in different shades of blue. Lighter shades correspond to smaller pericentres, as labelled. Solid lines show the circular velocity at the half-light radius,  $r_{1/2}$ , and dashed lines at the radius of maximum circular velocity,  $r_{\text{max}}$ . Symbols indicate the snapshot closest to  $t = 0$  which matches the current galactocentric distance of Fornax. The black solid line and grey shaded region correspond to the observational constraint on  $V_{1/2}$  as well as the  $\pm 1\sigma$  uncertainty interval as in Fattahi et al. (2018).



**Figure 5.** Initial and final circular velocity profiles of the Fornax halo for the three simulated orbits. The red contours are constraints on the enclosed mass within  $\sim 1$  kpc, derived from the stellar velocity dispersion and density profiles (see Fattahi et al. 2016a, for details). The grey band corresponds to the kinematic analysis of Read et al. (2019). Error bars with yellow centres show the estimates of Walker & Peñarrubia (2011), while the remaining three errorbars show the estimates of Amorisco et al. (2013). The dotted line shows an NFW profile with  $V_{\text{max}}$  and  $r_{\text{max}}$  as in the final circular velocity profile of Orbit 1. The transition from thick to thin lines indicate  $r_{\text{conv}}$ , the convergence radius defined in Section 2.4.

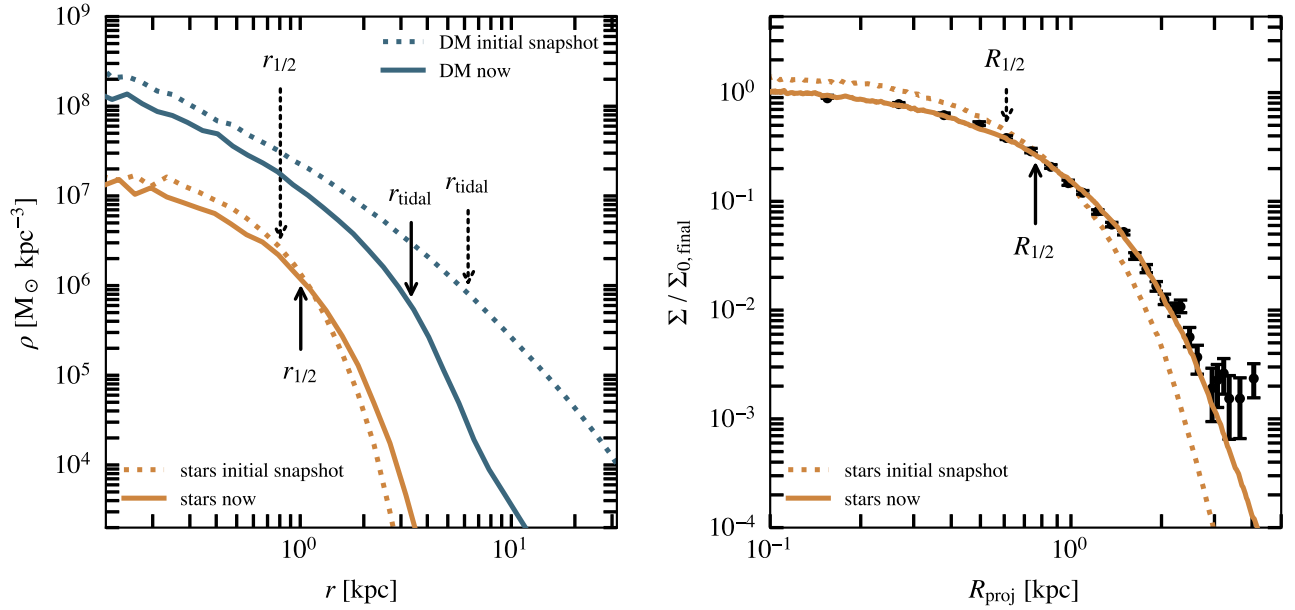


**Figure 6.** Left-hand panel: dark matter (blue) and stellar (orange) density profiles at infall (dotted curves) and after  $\sim 10$  Gyr on Orbit 1 (solid curves). Three dimensional half-mass and tidal radii are shown using arrows. Right-hand panel: surface brightness (orange curves, normalized to the final central value) profiles obtained from the  $N$ -body simulations, compared against the observational data by Coleman et al. (2005) (black data points). The projected (2D) half-light radii are shown using arrows. The stellar profile, being deeply embedded in the Fornax dark matter halo, is less affected by tides than the dark matter.

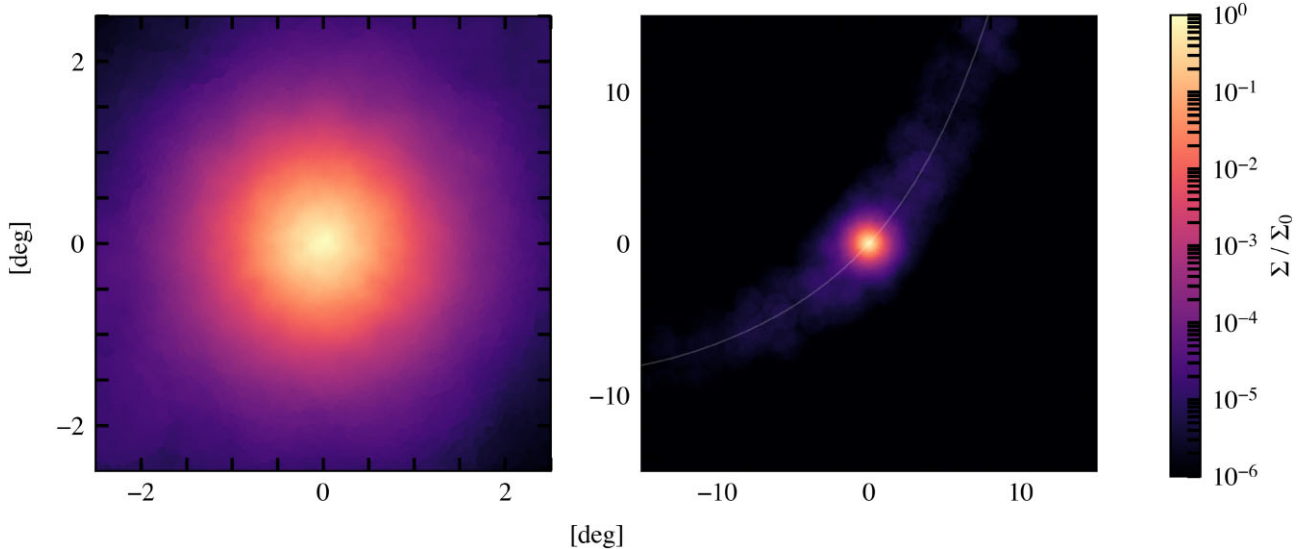


**Figure 7.** Surface brightness of the evolved Fornax model on Orbit 1. At a heliocentric distance of 137 kpc, one degree in this figure corresponds to 2.4 kpc. The left-hand panel shows an area of  $25 \text{ deg}^2$  centred on Fornax. Deviations from spherical symmetry in the surface brightness become only evident in regions where the surface brightness drops below  $1/1000$  of its central value. The panel on the right-hand shows a larger  $900 \text{ deg}^2$  areas and suggest the presence of a faint stellar stream. The line passing along the tidal stream in the right-hand panel indicates the orbital path of Fornax.

This becomes apparent when plotting a larger area around the dwarf (right-hand panel of Fig. 7), which shows the presence of a very faint stellar tidal stream, with a surface brightness more than 1000 times fainter than the central surface brightness of Fornax. The total stellar mass outside a sphere of radius 2 kpc is only  $2.6 \times 10^6 M_\odot$ , or approximately a tenth of Fornax’s initial stellar mass.

We conclude that, despite the large losses of dark matter due to stripping, the stellar component remains relatively undisturbed, and should show no obvious signatures of tidal disturbance. Signs of past tidal interaction may be present in the form of very low surface brightness tidal tails around the Fornax dwarf aligned roughly in the

direction of the orbital motion, as shown by the curve in the right-hand panel of Fig. 7. The discovery of such stars would provide strong support for the idea that tidal effects have played an important role in the dynamical evolution of Fornax.

### 3.3 Globular cluster orbital decay

We now focus our attention on the potential effects of tides on the orbital decay of the five GCs associated with the Fornax dSph. Meadows et al. (2020) have recently used  $N$ -body simulations to model the orbital decay of GCs in Fornax, modelled as a cuspy NFW



**Table 4.** Selected properties of Fornax GCs. Both projected radii and masses are taken from Mackey & Gilmore (2003).

Name	$R$ (kpc)	$\log M$ ( $M_\odot$ )
GC 1	1.60	$4.57 \pm 0.13$
GC 2	1.05	$5.26 \pm 0.12$
GC 3	0.43	$5.56 \pm 0.12$
GC 4	0.24	$5.12 \pm 0.24$
GC 5	1.43	$5.25 \pm 0.20$

halo. These authors argue that the GCs commonly referred to as GC3 and GC4 (see Table 4) are expected to sink to the centre of Fornax within the next  $\sim 2$  Gyr due to dynamical friction, while the remaining three clusters (GC1, GC2, and GC5) are too far from the centre of Fornax or have too little mass to decay, even in a time span as long as 15 Gyr. In agreement with earlier work (Angus & Diaferio 2009; Cole et al. 2012), these authors also conclude that even if GC3 and GC4 have experienced dynamical friction in a cuspy NFW halo for  $\sim 10$  Gyr, they could have avoided sinking to the centre if their initial orbital radii was 1–2 kpc.

The models of Meadows et al. (2020), however, neglect the effect of Galactic tides and assume a relatively low halo mass for Fornax, namely an NFW halo with  $V_{\max} = 25 \text{ km s}^{-1}$ , rather than the  $40 \text{ km s}^{-1}$  suggested by LCDM simulations. It is therefore important to explore whether their conclusions are robust to changes in the assumed halo mass, as well as to the inclusion of Galactic tides.

To this end, we add GCs to our Fornax models with  $10^7$  particles, including them as single softened point masses, with masses chosen to match the present-day mass of Fornax GCs, between  $3.7 \times 10^4$  and  $36 \times 10^4 M_\odot$  (Mackey & Gilmore 2003). The Plummer-equivalent softening length chosen for all GC particles is  $\epsilon_p = 13 \text{ pc}$ . Following Meadows et al. (2020), these clusters are placed on circular orbits at radii between 1 and 2 kpc and evolved first in isolation for 10 Gyr.

The orbital decay of these objects in isolation is shown by the grey lines in Fig. 8. GC1, GC2, and GC5 evolve very little over 10 Gyr, so choosing initial orbital radii consistent with their present-day projected radii (indicated by the horizontal dashed lines) results in good agreement with their observed position after 10 Gyr. No

appreciable orbital decay is expected for any of these three GCs, at least when Fornax is evolved in isolation.

The situation is different for GC4 and GC3, the two clusters closest (in projection) to the centre of Fornax. Their deprojected 3D distance is shown by the bottom horizontal dashed lines in the left- and right-hand panels of Fig. 8, respectively. Because of their proximity to the centre and their relatively large masses, GC3 and GC4 decay more quickly, and they need to have started their orbital evolution at  $\sim 1.6$  and  $\sim 1.0 \text{ kpc}$ , respectively, in order to match their present-day position after  $\sim 10$  Gyr.

How does including Galactic tides change these conclusions? We explore this by evolving each GC again, but placing the Fornax model in orbit around the Milky Way. We focus here on Orbit 1, where the effects of tides are the strongest. The resulting evolution of each cluster is shown by the coloured lines in Fig. 8. Cluster orbits are significantly affected by Galactic tides; however, the main effect is to increase the GCs' orbital eccentricity, while their orbital decay time-scales remain much the same as in isolation. These results, thus, suggest that Galactic tides have only a minor effect on the dynamical friction evolution of GCs in Fornax over 10 Gyr, even in the case of a Galactic orbit with rather small pericentric distance.

The conclusions of Meadows et al. (2020) therefore appear to hold. Only GC3 and GC4 are expected to be affected by dynamical friction; their present-day positions are readily explained if their initial orbital radii was between 1–2 kpc. This is enough to reconcile the present-day radial distribution of GCs around Fornax with the cuspy dark matter halo profile expected in LCDM.

#### 4 SUMMARY AND CONCLUSIONS

We have used  $N$ -body simulations to study the evolution of the Fornax dSph in the Galactic potential. Our main goal is to explore whether Galactic tides may help (i) to explain the relatively low dark matter content of Fornax compared with that expected from LCDM cosmological hydrodynamical simulations of dwarf galaxy formation, and (ii) to reconcile the spatial configuration of its GCs with their apparently short dynamical friction orbital decay time-scales. Our model assumes that Fornax is a dark-matter dominated system embedded in a cuspy NFW halo. Our main conclusions may be summarized as follows.

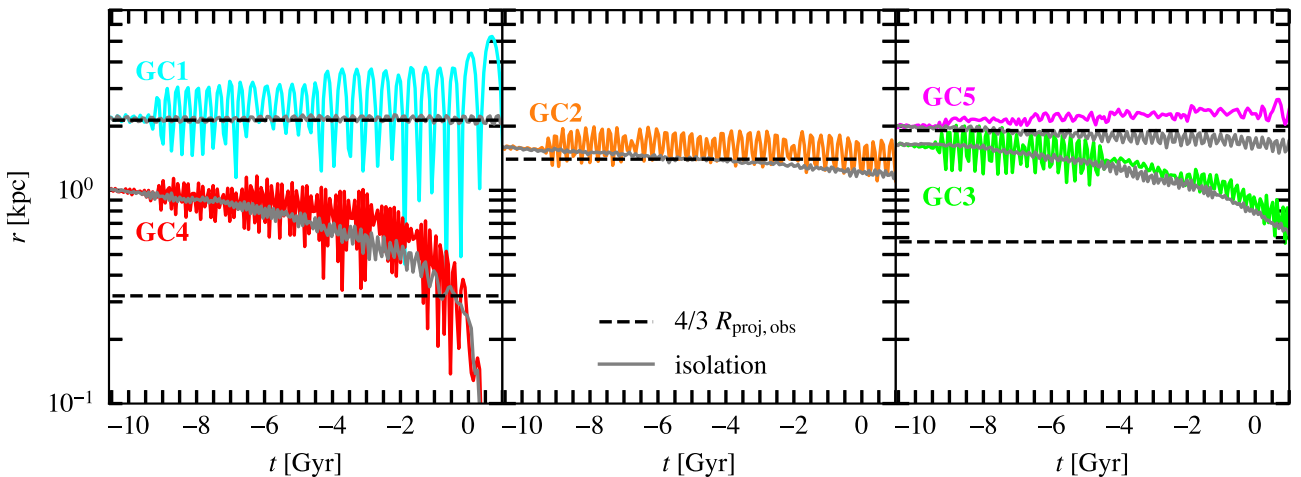


**Figure 8.** The evolution of the distance to the centre of Fornax for the five GCs. Coloured lines show the evolution in the presence of tides (orbit 1); grey curves correspond to runs in isolation. Initial radii are chosen so that in absence of tides, the GCs have decayed to approximately their currently observed projected radii in about 10 Gyr. The main effect of tides is to increase the GC orbital eccentricities (they are initially set on circular orbits); their effect on the orbital decay time-scales seems minor at best.

Using the latest available data on Fornax's sky position, distance, radial velocity, and proper motions, together with a Galactic potential model that matches the most recent dynamical constraints, we conclude that the pericentric distance of Fornax's orbit is only loosely constrained. The main reason for this is the particular direction of Fornax's orbital velocity at present, which is antiparallel to the Sun's Galactocentric velocity. This implies a large heliocentric tangential velocity, which translates into a sensitive dependence of Fornax's inferred Galactocentric velocity on its assumed distance. Indeed, a  $\pm 8$  per cent error in the distance translates into pericentric distances that may vary between  $\sim 50$  and  $130$  kpc.

Assuming a pericentric distance at the small end of that range, our models suggest that a Fornax NFW halo model with  $M_{200} = 1 \times 10^{10} M_{\odot}$  (or, equivalently,  $V_{\max} = 40 \text{ km s}^{-1}$ , consistent with the results of the APOSTLE suite of LCDM Local Group simulations) would be stripped of most of its dark mass over  $\sim 10$  Gyr of evolution (over four full orbits in the assumed Galactic potential). The tidal mass-loss would reduce  $V_{\max}$  to roughly  $\sim 23 \text{ km s}^{-1}$ , and the total enclosed mass within half-light radius of Fornax ( $r_{1/2} \approx 1$  kpc) by  $\sim 42$  per cent, bringing it into agreement with observational estimates.

Our models also indicate that most of the mass lost to stripping is *dark*, and that the total stellar component of Fornax is far less affected. Indeed, a stellar tracer modelled as a Sérsic model with  $n = 0.81$  and  $R_{1/2} = 0.61$  kpc (which matches fairly well the observed light profile of Fornax) would be hardly affected, losing less than 5 per cent of its mass in the process. Stripped stars would form tidal tails around Fornax, but with an average surface brightness more than 1000 times fainter than Fornax's central value and therefore extremely challenging to detect. Our models show that the stellar component of Fornax inside at least  $\sim 3$  kpc would show no obvious evidence of any tidal disturbance, again consistent with observations.

Similarly, the effect of Galactic tides on the dynamical friction decay times of Fornax's population of GCs is minor compared with models run in isolation. Thus, a population of GCs with initial orbital radii between 1 and 2 kpc is consistent with their present-day spatial distribution, despite assuming a cuspy NFW halo.

All models implemented here assume tidal stripping in Fornax due to the gravitational influence of the Milky Way only. We note that a massive nearby satellite as the LMC could have a non-negligible contribution to the gravitational potential felt by Fornax, modifying its orbital evolution from that presented here (see e.g. Erkal et al. 2019; Patel et al. 2020). Further uncertainties may arise from the still undetermined total mass of the Milky Way; the total mass considered in this work ( $M_{200} \sim 1.15 \times 10^{12} M_{\odot}$ ; McMillan 2011) lies slightly above recent estimates provided by studies based on LMC analogues in cosmological simulations of the Local Group (Santos-Santos et al. 2020) or stellar halo kinematics (Deason et al. 2021). We plan to consider these effects in future work.

We conclude that both the low dark matter content measured for the Fornax dSph and the radial distribution of its GC population are consistent with a scenario where Galactic tides are solely responsible for stripping a cuspy NFW halo with virial mass  $10^{10} M_{\odot}$ , as expected from abundance-matching arguments. Note that this scenario does not require a 'core' but it does require a relatively small pericentric distance ( $\sim 50$  kpc) for tides to operate effectively. This is possible if Fornax's true Galactocentric distance is slightly lower than, but within the uncertainty of, current estimates. A tighter distance estimate would therefore provide a helpful check to the validity of this scenario. A further check could be provided by tighter constraints on the innermost mass profile. In the tidal scenario proposed here, Fornax's halo is still cuspy; probes of the mass profile within a couple of hundred parsecs would be especially helpful in order to

settle questions about the presence of a core or a cusp in the Fornax dSph.

## ACKNOWLEDGEMENTS

This work used the DiRAC@Durham facility managed by the Institute for Computational Cosmology on behalf of the STFC DiRAC HPC Facility ([www.dirac.ac.uk](http://www.dirac.ac.uk)). The equipment was funded by BEIS capital funding via STFC capital grants ST/K00042X/1, ST/P002293/1, ST/R002371/1, and ST/S002502/1, Durham University and STFC operations grant ST/R000832/1. DiRAC is part of the National e-Infrastructure.

RE acknowledges support provided by a CITA National Fellowship and by funding from the European Research Council (ERC) under the European Unions Horizon 2020 research and innovation programme (grant agreement no. 834148).

AF is supported by a UKRI Future Leaders Fellowship (grant number MR/T042362/1) and Leverhulme Trust.

ISS is supported by the Arthur B. McDonald Canadian Astroparticle Physics Research Institute.

## DATA AVAILABILITY

The data underlying this article will be shared on reasonable request to the corresponding author.

## REFERENCES

- Amorisco N. C., Agnello A., Evans N. W., 2013, *MNRAS*, 429, L89  
 Angus G. W., Diaferio A., 2009, *MNRAS*, 396, 887  
 Battaglia G., Sollima A., Nipoti C., 2015, *MNRAS*, 454, 2401  
 Behroozi P. S., Wechsler R. H., Conroy C., 2013, *ApJ*, 770, 57  
 Benson A. J., Lacey C. G., Baugh C. M., Cole S., Frenk C. S., 2002, *MNRAS*, 333, 156  
 Bolchini P., Mohayaee R., Silk J., 2019, *MNRAS*, 485, 2546  
 Bullock J. S., Johnston K. V., 2005, *ApJ*, 635, 931  
 Bullock J. S., Kravtsov A. V., Weinberg D. H., 2000, *ApJ*, 539, 517  
 Cole D. R., Dehnen W., Read J. I., Wilkinson M. I., 2012, *MNRAS*, 426, 601  
 Coleman M. G., Da Costa G. S., Bland-Hawthorn J., Freeman K. C., 2005, *AJ*, 129, 1443  
 Deason A. J. et al., 2021, *MNRAS*, 501, 5964  
 Di Cintio A., Brook C. B., Macciò A. V., Stinson G. S., Knebe A., Dutton A., Wadsley J., 2014, *MNRAS*, 437, 415  
 Dinescu D. I., Keeney B. A., Majewski S. R., Girard T. M., 2004, *AJ*, 128, 687  
 Einasto J., 1965, Tr. Astrofizicheskogo Inst. Alma-Ata, 5, 87  
 Erkal D. et al., 2019, *MNRAS*, 487, 2685  
 Errani R., Navarro J. F., 2020, *MNRAS*, 505, 18  
 Errani R., Peñarrubia J., 2020, *MNRAS*, 491, 4591  
 Fattahi A., Navarro J. F., Sawala T., Frenk C. S., Sales L. V., Oman K., Schaller M., Wang J., 2016a, preprint ([arXiv:1607.06479](https://arxiv.org/abs/1607.06479))  
 Fattahi A. et al., 2016b, *MNRAS*, 457, 844  
 Fattahi A., Navarro J. F., Frenk C. S., Oman K. A., Sawala T., Schaller M., 2018, *MNRAS*, 476, 3816  
 Forbes D. A., Read J. I., Gieles M., Collins M. L. M., 2018, *MNRAS*, 481, 5592  
 Fritz T. K., Battaglia G., Pawlowski M. S., Kallivayalil N., van der Marel R., Sohn S. T., Brook C., Besla G., 2018, *A&A*, 619, A103  
 et al., 2018, *A&A*, 616, A12  
 Garrison-Kimmel S. et al., 2019, *MNRAS*, 487, 1380  
 Genina A., Read J. I., Fattahi A., Frenk C. S., 2020, preprint ([arXiv:2011.09482](https://arxiv.org/abs/2011.09482))  
 Goerdt T., Moore B., Read J. I., Stadel J., Zemp M., 2006, *MNRAS*, 368, 1073

- Guo Q., White S., Li C., Boylan-Kolchin M., 2010, *MNRAS*, 404, 1111
- Hayashi E., Navarro J. F., Taylor J. E., Stadel J., Quinn T., 2003, *ApJ*, 584, 541
- Hernandez X., Gilmore G., 1998, *MNRAS*, 297, 517
- Hernquist L., 1990, *ApJ*, 356, 359
- Irwin M., Hatzidimitriou D., 1995, *MNRAS*, 277, 1354
- Ludlow A. D., Bose S., Angulo R. E., Wang L., Hellwing W. A., Navarro J. F., Cole S., Frenk C. S., 2016, *MNRAS*, 460, 1214
- Mackey A. D., Gilmore G. F., 2003, *MNRAS*, 340, 175
- McConnachie A. W., 2012, *AJ*, 144, 4
- McMillan P. J., 2011, *MNRAS*, 414, 2446
- Meadows N., Navarro J. F., Santos-Santos I., Benítez-Llambay A., Frenk C., 2020, *MNRAS*, 491, 3336
- Miyamoto M., Nagai R., 1975, *PASJ*, 27, 533
- Moster B. P., Naab T., White S. D. M., 2013, *MNRAS*, 428, 3121
- Munshi F., Brooks A., Applebaum E., Christensen C., Sligh J. P., Quinn T., 2021, preprint ([arXiv:2101.05822](https://arxiv.org/abs/2101.05822))
- Navarro J. F., Eke V. R., Frenk C. S., 1996, *MNRAS*, 283, L72
- Navarro J. F., Frenk C. S., White S. D. M., 1997, *ApJ*, 490, 493
- Oh K. S., Lin D. N. C., Richer H. B., 2000, *ApJ*, 531, 727
- Patel E. et al., 2020, *ApJ*, 893, 121
- Peñarrubia J., Navarro J. F., McConnachie A. W., 2008, *ApJ*, 673, 226
- Petts J. A., Gualandris A., Read J. I., 2015, *MNRAS*, 454, 3778
- Piatek S. et al., 2002, *AJ*, 124, 3198
- Pietrzyński G., Górski M., Gieren W., Ivanov V. D., Bresolin F., Kudritzki R.-P., 2009, *AJ*, 138, 459
- Planck Collaboration et al., 2016, *A&A*, 594, A13
- Pontzen A., Governato F., 2012, *MNRAS*, 421, 3464
- Read J. I., Gilmore G., 2005, *MNRAS*, 356, 107
- Read J. I., Goerdt T., Moore B., Pontzen A. P., Stadel J., Lake G., 2006, *MNRAS*, 373, 1451
- Read J. I., Walker M. G., Steger P., 2019, *MNRAS*, 484, 1401
- Santos-Santos I. M. E., Fattahi A., Sales L. V., Navarro J. F., 2020, *MNRAS*, 504, 4551
- Sawala T. et al., 2016, *MNRAS*, 457, 1931
- Schaye J. et al., 2015, *MNRAS*, 446, 521
- Schönrich R., Binney J., Dehnen W., 2010, *MNRAS*, 403, 1829
- Sersic J. L., 1968, *Atlas de Galaxias Australes*. Observatorio Astronomico, Cordoba, Argentina
- Shao S., Cautun M., Frenk C. S., Reina-Campos M., Deason A. J., Crain R. A., Kruijssen J. M. D., Pfeffer J., 2020, *MNRAS*, 507, 2339
- Somerville R. S., 2002, *ApJ*, 572, L23
- Springel V., 2005, *MNRAS*, 364, 1105
- Tremaine S. D., 1976, *ApJ*, 203, 345
- Vogelsberger M. et al., 2014, *MNRAS*, 444, 1518
- Walker M. G., Peñarrubia J., 2011, *ApJ*, 742, 20
- Walker M. G., Mateo M., Olszewski E. W., 2009, *AJ*, 137, 3100
- Wang M. Y. et al., 2019, *ApJ*, 881, 118
- Wang L., Dutton A. A., Stinson G. S., Macciò A. V., Penzo C., Kang X., Keller B. W., Wadsley J., 2015, *MNRAS*, 454, 83
- White S. D. M., Rees M. J., 1978, *MNRAS*, 183, 341
- Wolf J., Martinez G. D., Bullock J. S., Kaplinghat M., Geha M., Muñoz R., Simon J. D., Avedo F. F., 2010, *MNRAS*, 406, 1220
- Woo J., Courteau S., Dekel A., 2008, *MNRAS*, 390, 1453

This paper has been typeset from a  $\mathrm{\LaTeX}$  file prepared by the author.